Journal of Alloys and Compounds 1027 (2025) 180504

Contents lists available at ScienceDirect

Journal of Alloys and Compounds

journal homepage: www.elsevier.com/locate/jalcom

Strategic approach to simultaneously enhance strength, formability, and corrosion-resistance synergy of age-hardenable Mg-Zn-Ca-Al-Mn alloy sheet with low Mn content *via* optimizing Zn and Ca contents

K. Kikuchi [a], T. Nakata [a,*], Z.H. Li [b], T.T. Sasaki [b], Y. Miyashita [a], S. Kamado [a]

[a] *Nagaoka University of Technology, 1603-1, Kamitomioka, Nagaoka 940-2188, Japan*
[b] *National Institute for Materials Science, 1-2-1 Sengen, Tsukuba 305-0047, Japan*

ARTICLE INFO

Keywords:
Mg-Zn-Ca-Al-Mn alloy
Rolling
Age-hardening
Tensile property
Corrosion resistance

ABSTRACT

To develop a strong, room-temperature (RT)-formable, and corrosion-resistant Mg alloy sheet, we investigate the age-hardening response, RT formability, tensile properties, and corrosion resistance of low-Mn-containing Mg-(1, 2)Zn-(0.2, 0.5, 1)Ca-0.2Al-0.2Mn (ZXAM, mass%) alloy sheets. The Zn content minimally affects the above-mentioned properties. However, the Ca content is important for significantly improving the properties. The addition of $\geq$ 0.5mass%Ca enhances the RT formability by inclining the (0001) poles toward the transverse direction. Dense corrosion products are formed on the surface of the $\geq$ 0.5mass%Ca-containing ZXAM alloy sheets, resulting in improved corrosion resistance. Moreover, the aged $\geq$ 0.5mass%Ca-containing ZXAM alloy sheets exhibit high strength along the rolling direction (RD), in which the 0.2 % proof strength (PS) exceeds 200 MPa. Aging-treatment reduces the corrosion resistance slightly, although the corrosion rates are lower compared with those of commercial wrought Mg alloys. Thereafter, a Mg-2Zn-0.5Ca-0.2Al-0.2Mn alloy sheet simultaneously achieves an excellent combination of strength, RT formability, and corrosion resistance *via* age-hardening. The PS along the RD and the Index Erichsen value of the sheet reached 213 MPa and 8.7 mm, respectively, and its corrosion rate after immersion in 3.5mass%NaCl solution for 3 days is 3.0 mm$\cdot$y^{-1}.

1. Introduction

Magnesium and its sheet alloys are promising candidates as next-generation lightweight materials for the automotive industry [1–3]. However, the widespread use of Mg sheet alloys is hindered by their low corrosion resistance; moreover, simultaneously improving their strength and room-temperature (RT) formability is challenging [1–3]. The insufficient strength and RT formability are primarily caused by the texture features. Mg-3mass%Al-1mass%Zn-Mn (AZ31), which is a typical wrought Mg alloy, shows a strong basal texture with the (0001) poles aligned to the normal direction (ND) [3–5], resulting in poor RT formability, and their Index Erichsen (I.E.) values are 3–5 mm [2–5]. The I.E. values of commercial Al sheet alloys are 10–11 mm, which are 2–3 times higher than those of AZ31 sheets [6,7].

The inclination of (0001) poles from the ND can be achieved by rolling at high temperatures. However, such textural features decrease the 0.2 % proof strength (PS). An AZ31 sheet shows an I.E. value of 4.5 mm and PSs of 165 and 173 MPa for the rolling direction (RD) and transverse direction (TD), respectively, after being rolled at a moderate temperature of 450 °C. By contrast, rolling at a high temperature of 525 °C results in an enhanced I.E. value of 8.6 mm, whereas the PSs along the RD and TD decrease to 144 and 154 MPa, respectively [4].

Optimization of alloying elements is another method for inclining (0001) poles. In particular, strong and RT-formable Mg alloy sheets have been successfully designed without expensive rare-earth elements [2,3,8]. Recently, Mg-Zn-Ca-Al-Mn (ZXAM) alloys have become promising materials for extruded [9–12] and rolled [13–17] products because of their excellent mechanical properties and cost-effectiveness. Huang et al. demonstrated that a rolled Mg-3Zn-0.5Ca-0.5Al-1Mn (mass%) alloy sheet exhibited a high I.E. value of 8.5 mm and a PS of 223 MPa along the RD [15]. The high I.E. value results from TD-split textural features, in which the (0001) poles were inclined toward the TD by the addition of Zn and Ca. By contrast, the high PS was due to grain refinement by Al-Mn precipitates, which exerted a pinning effect on the grain boundaries. However, the Al-Mn precipitates promoted galvanic corrosion between the Mg matrix, which significantly deteriorated the

---

* Corresponding author.
E-mail address: nakata@mech.nagaokaut.ac.jp (T. Nakata).

https://doi.org/10.1016/j.jallcom.2025.180504
Received 14 February 2025; Received in revised form 16 April 2025; Accepted 17 April 2025

Table 1
Nomenclatures and nominal compositions of Mg-Zn-Ca-Al-Mn alloy ingots used in this work (mass%). Actual chemical compositions measured by inductively coupled plasma method are provided in parentheses.

Alloy	Zn	Ca	Al	Mn
ZXAM1000(0.2Ca)	1 (0.99)	0.2 (0.15)	0.2 (0.24)	0.2 (0.23)
ZXAM2000(0.2Ca)	2 (1.77)	0.2 (0.18)	0.2 (0.23)	0.2 (0.21)
ZXAM1100(0.5Ca)	1 (0.84)	0.5 (0.58)	0.2 (0.21)	0.2 (0.15)
ZXAM2100(0.5Ca)	2 (2.02)	0.5 (0.53)	0.2 (0.24)	0.2 (0.23)
ZXAM1100(1Ca)	1 (0.89)	1 (1.08)	0.2 (0.20)	0.2 (0.31)
ZXAM2100(1Ca)	2 (1.96)	1 (1.07)	0.2 (0.20)	0.2 (0.24)

corrosion resistance [17–19]. Because corrosion resistance is an important factor for the application of automotive panel products, such as door panels and roofs, the amount of precipitates must be reduced by decreasing the Mn content [15,17]. Meanwhile, a low Mn content is expected to decrease the PS owing to grain coarsening [13,15].

Dilute Mg-Zn-Ca-based alloys form Guinier-Preston (G.P.) zones and exhibit substantial age-hardening under the appropriate contents of Zn and Ca. However, the excess Zn and Ca additions reduce the age-hardenability by suppressing the formation of G.P. zones. Therefore, the Zn and Ca contents should not exceed 2mass% and 1mass%, respectively [20–23]. We expect that even low-Mn-containing ZXAM alloy sheets will show high PS by maximizing age-hardenability; in this regard, the Zn and Ca contents must be optimized. In this work, the effects of Zn and Ca contents on the age-hardenability, RT formability, tensile properties, and corrosion properties of a low-Mn-containing ZXAM alloy sheet are investigated to design a high-performance Mg alloy sheet.

2. Experimental procedure

Mg-(1, 2)Zn-(0.2, 0.5, 1)Ca-0.2Al-0.2Mn (mass%) alloy ingots were prepared by gravity casting. The nomenclatures and nominal compositions of these alloys are summarized in Table 1. The inductively coupled plasma (ICP) method was used to evaluate the actual chemical composition. The compositions are listed in parentheses in Table 1, and an overview of our work is illustrated in Fig. 1. Rectangular-shaped plates measuring 60 mm × 100 mm × 6 mm were sectioned from the cast ingots, and the plates were homogenized at 390 °C for 6 hours and then air-cooled. Before rolling, the plates were preheated at 350 °C for 20 min in an electronic furnace, followed by air-cooling until the temperature of the surface of the sample reached 200 °C. Subsequently, the plates were rolled to obtain ~1-mm-thick sheets. The roller temperature and speed were fixed at 200 °C and 5 m/min, respectively. The thickness reduction per pass was ~30 %, and the preheating and rolling were repeated five times. Solution-treatment was conducted at 420 °C for 30 min after rolling, and the sheets were cooled by water quenching.

The changes in hardness during age-hardening at 170 °C were evaluated using a Micro Vickers hardness testing machine (Mitutoyo/HM-221). The solution-treated samples were soaked in a silicon oil bath, and their hardness was measured after aging for 0–512 hours. The average hardness was calculated based on five indentations at each aging time. Erichsen cupping tests were performed using solution-treated rectangular specimens with a dimension of 60 mm × 60 mm to evaluate the stretch formability at room-temperature (RT). An Erichsen cupping testing machine (ERICHSEN/Model 100) having a 20-mm-dia. hemispheric punch and blank-holder force of 10 kN was used. The testing speed was ~6 mm/min, and a 0.05-mm-thick Teflon sheet was inserted to reduce the friction between the punch and specimen. A universal testing machine (Shimadzu/Autograph AG-50kN) and specimens with a gauge length and width of 20 and 4 mm, respectively, were used to investigate the tensile properties. The tensile direction was parallel to the RD and TD, and the initial strain rate was 10^{-3} s^{-1}. The corrosion resistance was evaluated by an immersion test using NaCl solution at 20 °C (RT). For the immersion tests, 200 ml of 3.5mass%NaCl water was prepared, and each sample was immersed for 3 days. The volume of hydrogen gas was measured using a device similar to that used in a previous study [24], and the volume was converted to the corrosion rate. For the immersion test, 1-mm-thick rectangular samples with a length and width of ~10 mm were prepared by polishing using up to #4000 SiC grid papers. The polished samples were rinsed with ethanol and stored in a vacuum box for 1 day. Both the tensile and corrosion tests were conducted at least three times using both solution-treated and aged specimens.

The microstructure was characterized using a scanning electron microscope (JEOL/JSM-7000F) equipped with an electron

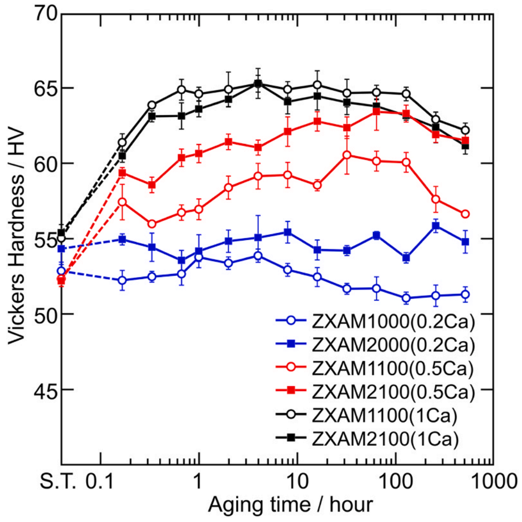

Fig. 2. Age-hardening response at 170 °C. S.T. represents solution-treated state.

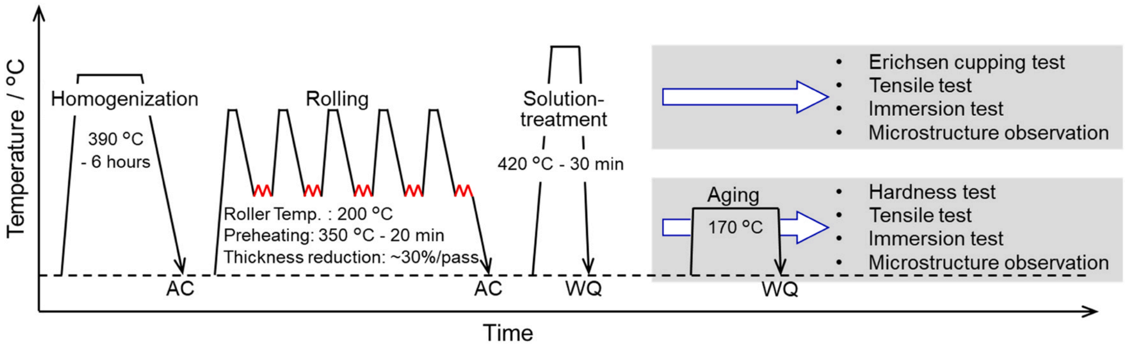

- Erichsen cupping test
- Tensile test
- Immersion test
- Microstructure observation

- Hardness test
- Tensile test
- Immersion test
- Microstructure observation

Fig. 1. Schematic illustration of current work.

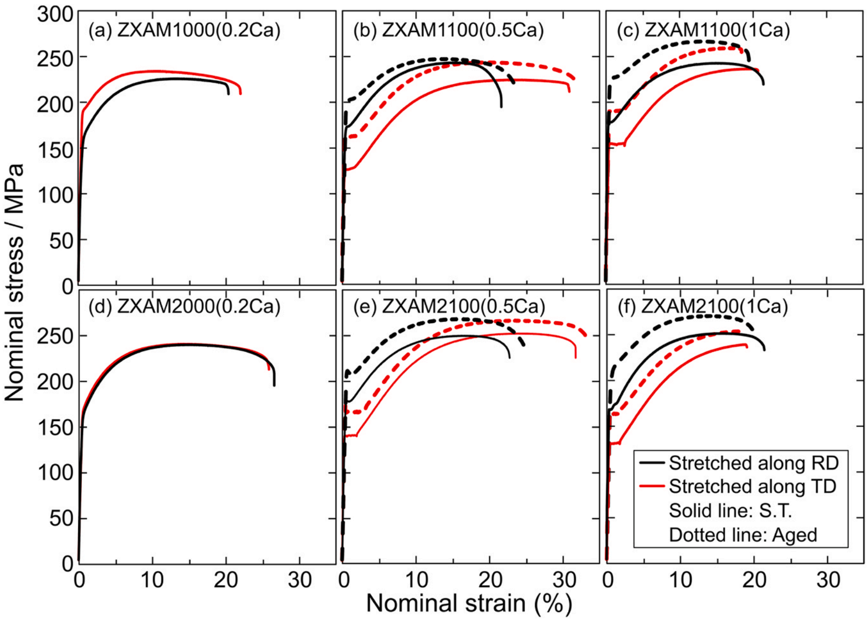

Fig. 3. Nominal stress-strain curves of solution-treated and aged samples; (a) ZXAM1000(0.2Ca), (b) ZXAM1100(0.5Ca), (c) ZXAM1100(1Ca), (d) ZXAM2000 (0.2Ca), (e) ZXAM2100(0.5Ca), and (f) ZXAM2100(1Ca) samples. S.T. represents solution-treated state.

Table 2

Tensile properties of solution-treated (S.T.) and aged samples. 0.2 % proof strength, ultimate tensile strength, elongation to failure, and ratio of PSs along RD and TD are labeled PS, UTS, EF, and PS_{TD}/PS_{RD}, respectively.

Alloy	State	Tension // RD			Tension // TD			PS_{TD}/PS_{RD}
		PS MPa	UTS MPa	EF (%)	PS MPa	UTS MPa	EF (%)	
ZXAM1000(0.2Ca)	S.T.	164 ± 5	231 ± 4	19.9 ± 1.7	187 ± 4	236 ± 2	20.6 ± 2.9	1.14
ZXAM2000(0.2Ca)	S.T.	167 ± 5	245 ± 4	22.5 ± 2.7	167 ± 3	243 ± 3	22.9 ± 1.9	1.00
ZXAM1100(0.5Ca)	S.T.	171 ± 2	242 ± 4	22.9 ± 1.9	130 ± 3	227 ± 3	28.8 ± 1.7	0.76
	Aged	205 ± 1	255 ± 0	18.2 ± 1.5	161 ± 1	242 ± 1	30.1 ± 1.4	0.79
ZXAM2100(0.5Ca)	S.T.	186 ± 3	264 ± 5	23.0 ± 2.4	139 ± 0	250 ± 1	29.7 ± 1.9	0.75
	Aged	213 ± 1	270 ± 2	24.4 ± 1.6	165 ± 1	265 ± 1	29.4 ± 1.8	0.77
ZXAM1100(1Ca)	S.T.	181 ± 3	240 ± 5	19.7 ± 1.1	152 ± 2	237 ± 1	18.9 ± 2.5	0.84
	Aged	225 ± 3	266 ± 2	19.1 ± 0.1	190 ± 0	258 ± 1	17.9 ± 1.0	0.84
ZXAM2100(1Ca)	S.T.	169 ± 4	252 ± 2	20.4 ± 1.9	133 ± 2	241 ± 2	20.1 ± 2.2	0.79
	Aged	204 ± 3	266 ± 3	19.7 ± 0.7	162 ± 2	252 ± 3	17.3 ± 2.2	0.79

backscattered diffraction (EBSD) apparatus (TSL), scanning electron microscopes (Carl Zeiss/Crossbeam 550 and JEOL/JSM-IT500 InTouchScope™) equipped with energy dispersive X-ray spectroscopy (EDS) detectors (Oxford Instruments/Ultim Max and JEOL/JED-2300), and a transmission electron microscope (FEI/Tecnai 20). For scanning electron microscopy (SEM) observations, the samples were metallographically prepared using SiC grid paper, Al_2O_3 powder, and colloidal silica suspensions. For transmission electron microscopy (TEM) observations, thin foils with a thickness of ~100 μm were prepared using mechanical polishing using #4000 grid papers and electro-polishing (Struers/Tenupol-5) at ~-50 °C in a mixture of 1500-ml-CH_4O (methanol), 300-ml-$C_6H_{14}O_2$ (2-butoxy ethanol), 33.5-g-$Mg(ClO_4)_2$ (magnesium perchlorate), and 15.9-g-LiCl (lithium chloride). After the electropolishing was completed, the thin foils were cleaned by ion milling (Gatan/Model691).

3. Results

Fig. 2 shows the variations in the Vickers hardness values as a function of the aging time. The solution-treated state is labeled as S.T. in Fig. 2. The hardnesses of all the sheets were similar, 52–55 HV, after the solution-treatment. The 0.2 %Ca-containing sheets did not show the increment in the hardness. By contrast, the hardness of the ≥ 0.5 %Ca-containing sheets increased gradually as aging progressed. The hardness of the ZXAM1100(0.5Ca) sheet reached the peak value after aging for 32 hours. The peak hardness was ~61 HV, and its hardness increment was ~8 HV. For the ZXAM2100(0.5Ca) sheet, a hardness increment was ~11 HV, and the time to reach the peak value was 64 hours. The 1 %Ca-containing sheets reached their peak hardness values faster than the 0.5 %Ca-containing sheets while indicating a hardness increment of ~10 HV after aging for 4 hours. Meanwhile, the hardness increments of the ZXAM1100(0.5Ca) and ZXAM2100(0.5Ca) sheets after aging for 4 hours were ~7 and ~9 HV, respectively. These values were similar to their maximum hardness increments, which were obtained after aging for 32 and 64 hours, respectively. Therefore, aging-treatment was performed for 4 hours on the ≥ 0.5 %Ca-containing sheets, whereas the aging-treatment was not performed on the 0.2 %Ca-containing sheets.

Fig. 3 shows the stress-strain curves during the tensioning of the solution-treated and aged samples. Table 2 summarizes the 0.2 % proof strength (PS), ultimate tensile strength (UTS), elongation to failure (EF), and ratio of PSs along the RD and TD (PS_{TD}/PS_{RD}). The solution-treated 0.2 %Ca-containing samples indicated PSs of 170–190 MPa and isotropic ductility, with the EFs of ~20 %. The addition of ≥ 0.5 %Ca decreased the PSs along the TD, thus resulting in a large in-plane anisotropy with a PS_{TD}/PS_{RD} of ~0.8. Moreover, the addition of ≥ 0.5 %Ca resulted in an apparent plateau region at yielding. The TD-

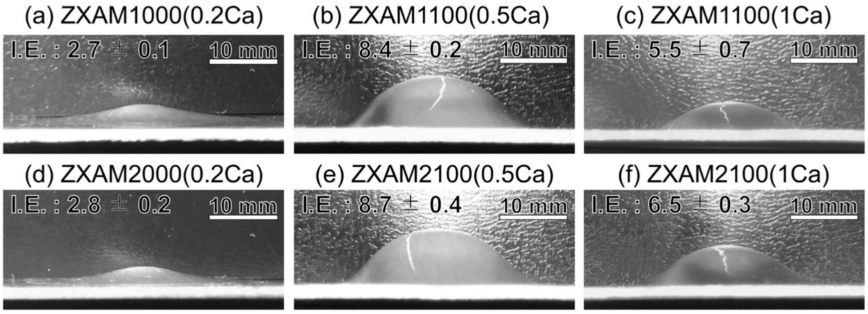

Fig. 4. Appearance of solution-treated samples after Erichsen cupping test; (a) ZXAM1000(0.2Ca), (b) ZXAM1100(0.5Ca), (c) ZXAM1100(1Ca), (d) ZXAM2000 (0.2Ca), (e) ZXAM2100(0.5Ca), and (f) ZXAM2100(1Ca) samples.

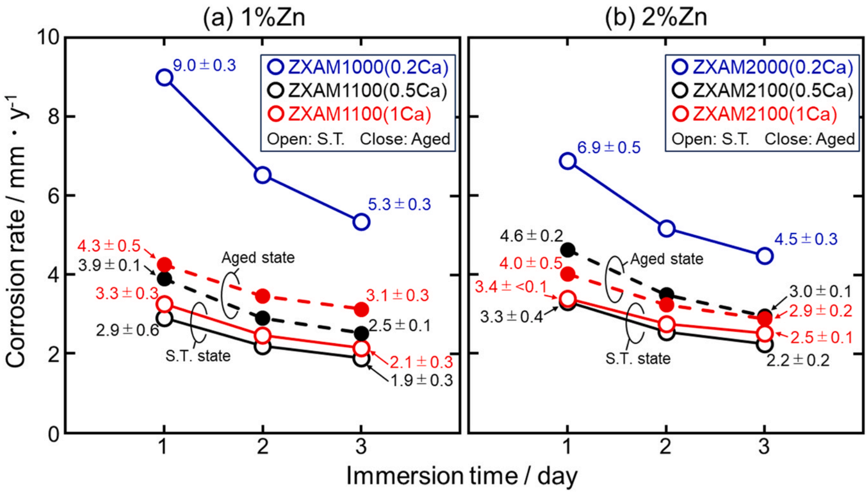

Fig. 5. Transitions of corrosion rates of solution-treated and aged samples during 3.5 %NaCl immersion test; (a) 1 %Zn-containing and (b) 2 %Zn-containing samples. S.T. represents solution-treated state.

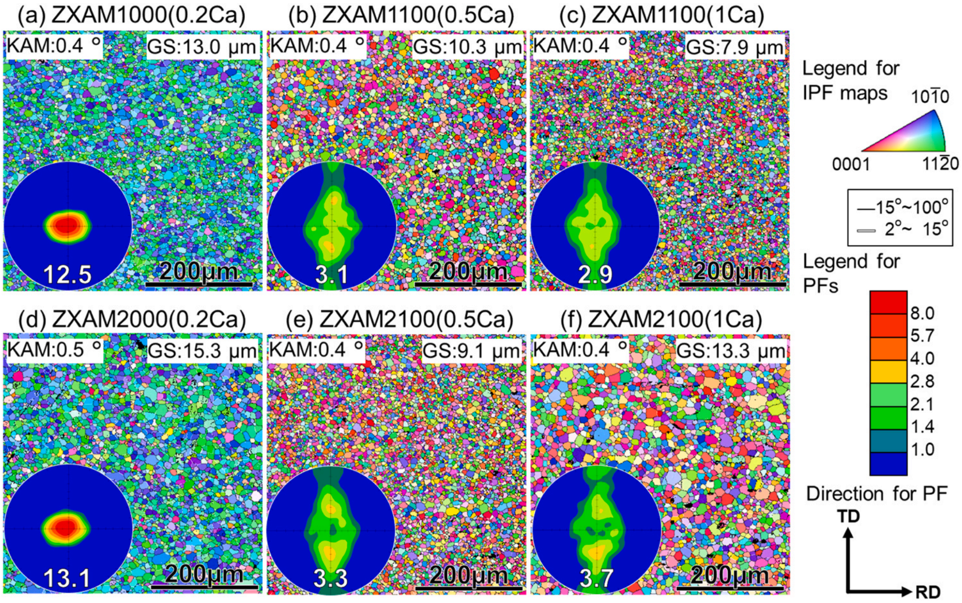

Fig. 6. IPF maps and (0001) PFs of solution-treated (a) ZXAM1000(0.2Ca), (b) ZXAM1100 (0.5Ca), (c) ZXAM1100(1Ca), (d) ZXAM2000(0.2Ca), (e) ZXAM2100 (0.5Ca), and (f) ZXAM2100(1Ca) samples. GS and KAM in each IPF map represent average grain size and Kernel average misorientation, respectively. Maximum intensity of (0001) poles is described in each (0001) PF.

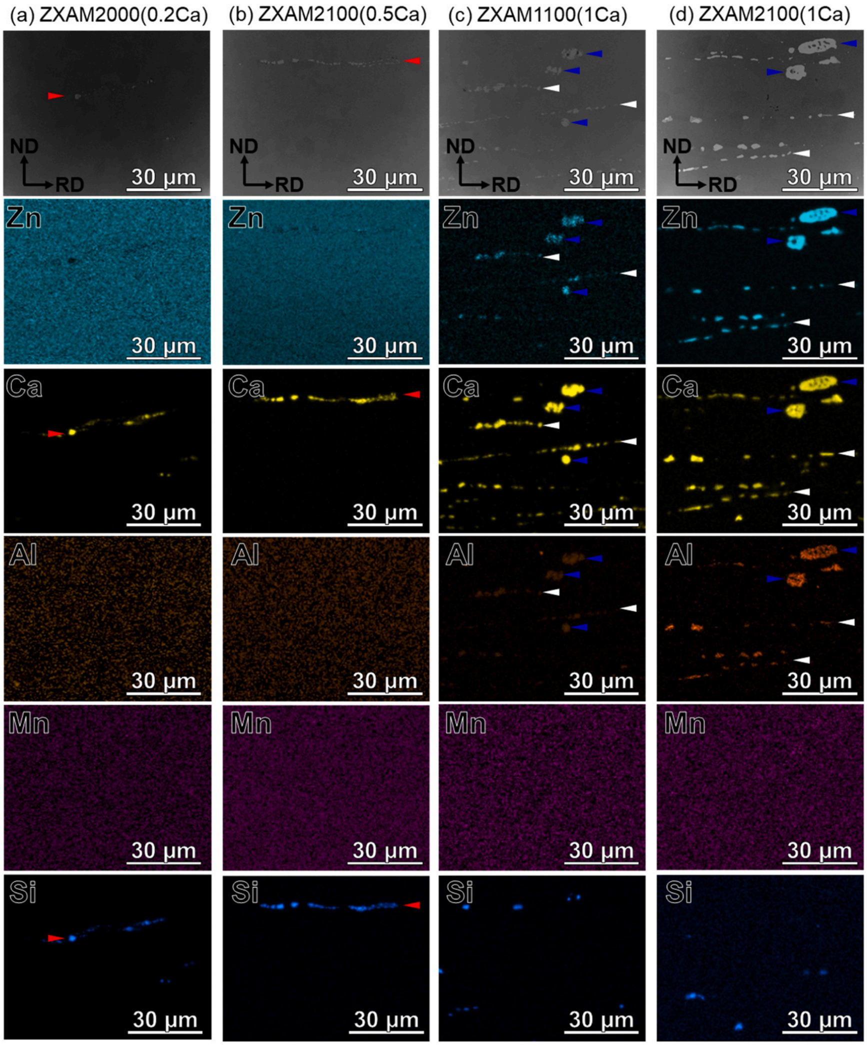

Fig. 7. BSE images and EDS elemental maps for Zn, Ca, Al, Mn, and Si obtained from solution-treated (a) ZXAM2000(0.2Ca), (b) ZXAM2100(0.5Ca), (c) ZXAM1100 (1Ca), and (d) ZXAM2100(1Ca) samples.

tension showed relatively large plateau regions compared to those of the RD-tension. The addition of 1 %Ca decreased the EFs, and the decrements in the EF for the RD and TD were ~3 % and ~10 %, respectively. The PSs for both the RD and TD increased by 30–40 MPa after aging. Consequently, the aged samples showed high PSs for RD of > 200 MPa. Moreover, aging did not lead to ductility loss.

Fig. 4 shows the appearance of the Erichsen cupping test specimens. The insets in the images indicate their average Index Erichsen (I.E.) values. The 0.2 %Ca-containing samples showed the poor I.E. values of ~3 mm. The addition of 0.5 %Ca significantly improved the RT formability. In particular, the ZXAM2100(0.5Ca) sheet exhibited the best I.E. value of 8.7 mm, which is comparable to that of Al alloy sheets [6,7], whereas the I.E. values were ~6.0 mm after the excess addition of 1 % Ca.

Fig. 5 shows the corrosion rates evaluated by the 3.5mass%NaCl immersion test. The corrosion rate of the ZXAM1000(0.2Ca) sample was 5.3 $\text{mm} \cdot \text{y}^{-1}$ after the immersion for 3 days, which was fastest among all the sheets. Meanwhile, the 2 %Zn addition to the 0.2 %Ca-containing sample slightly improved the corrosion rate to 4.5 $\text{mm} \cdot \text{y}^{-1}$, which was faster than those of the other sheets. Meanwhile, the ≥ 0.5 %Ca addition significantly improved the corrosion resistance. The corrosion rates of the solution-treated 0.5 %Ca- and 1 %Ca-containing samples were 2.0–2.5 $\text{mm} \cdot \text{y}^{-1}$ after immersion for 3 days. All the aged 0.5 %Ca- and 1 %Ca-containing samples showed relatively high corrosion rates of 2.5–3.0 $\text{mm} \cdot \text{y}^{-1}$, which are still better than that of a typical wrought Mg alloy (AZ31) [25].

Fig. 6 shows the inverse pole figure (IPF) maps and (0001) pole figures (PFs) obtained from the solution-treated sheets. The average grain size and Kernel average misorientation value are donated as GS and KAM, respectively, in the IPF maps. The maximum intensities of the poles are described in the (0001) PFs. Except for the ZXAM2100(1Ca) sample, the grain size was refined with increasing the Ca content owing to grain boundary pinning by the particles [26,27]. The grain sizes of the 0.5 %Ca-containing and ZXAM1100(1Ca) samples were 8–10 μm. The 0.2 %Ca-containing samples exhibited a strong basal texture, and their maximum intensities were > 10 m.r.d. (multiples of random distribution). The ≥ 0.5 %Ca-containing samples showed a TD-split texture and low maximum intensities of 3–4 m.r.d. The KAM values for all the samples were below 0.5 °, thus indicating that all the samples consisted of fully recrystallized grains with a limited density of dislocations [28].

Fig. 7 shows backscattered electron (BSE) images of the solution-treated (a) ZXAM2000(0.2Ca), (b) ZXAM2100(0.5Ca), (c) ZAM1100 (1Ca), and (d) ZXAM2100(1Ca) samples. The corresponding EDS elemental maps are shown in Fig. 7(a–d). As indicated by the red arrowheads, the ZXAM2000(0.2Ca) and ZXAM2100(0.5Ca) samples comprised particles that were aligned with the RD. They were enriched with Ca and Si, which indicates the formation of a MgCaSi phase (orthorhombic structure, a = 0.748 nm, b = 0.440 nm, c = 0.829 nm)

Table 3
EDS point analysis results (at%) obtained from large and aligned particles of 1 % Ca-containing samples.

Alloy	Particle type	Zn	Ca	Al	Mn	Si
ZXAM1100 (1Ca)	Large	1.3 ± 0.2	25.2 ± 5.5	3.1 ± 0.5	< 0.1	< 0.1
	Aligned	1.0 ± 0.1	15.7 ± 2.4	1.8 ± 0.3	< 0.1	< 0.1
ZXAM2100 (1Ca)	Large	12.1 ± 2.5	16.9 ± 3.5	3.1 ± 0.2	< 0.1	< 0.1
	Aligned	12.6 ± 1.3	14.0 ± 1.8	2.9 ± 0.3	< 0.1	< 0.1

[29,30]. As indicated by the white arrowheads, the addition of 1 %Ca increased the number of particles that were aligned with the RD. Moreover, the 1 %Ca-containing samples comprised large particles with a diameter of ~10 μm, as indicated by the blue arrowheads. A few particles contained Ca and Si, thus indicating the formation of a MgCaSi phase, whereas Ca was the main constituent in the particles of the ZXAM1100(1Ca) sample. Similarly, the ZXAM2100(1Ca) sample contained some types of particles. As indicated by the white arrowheads, some of the particles, whose diameters were < 10 μm, appeared along the RD. Meanwhile, the other particles were relatively large, with diameters of 10–15 μm, as indicated by the blue arrowheads. To identify large and aligned particles in the 1 %Ca-containing samples, EDS point analyses were conducted on the particles, as summarized in Table 3. The analysis was repeated five times to calculate the average values. The large and aligned particles in the ZXAM1100(1Ca) sample primarily consisted of Ca and trace amounts of Zn and Al. They belonged to the Mg_2Ca (hexagonal, a = 0.62 nm, c = 1.0 nm) phase, in which trace amounts of Zn and Al are dissolved [29,31]. In the ZXAM2100(1Ca) sample, the compositions of both large and aligned particles were nearly identical. The Zn and Ca contents were 12–13 at% and 14–17 at%, respectively. In fact, ~3 at%Al was dissolved in the particles. This indicates the formation of a $Ca_2Mg_6Zn_3$ phase (trigonal, a = 0.97 nm, c = 1.0 nm), in which a trace amount of Al was dissolved [32,33]. These results show that the particle type in the 1 %Ca-containing samples is influenced by the Zn content.

Fig. 8 shows the high-magnification BSE images of the solution-treated (a) ZXAM2100(0.5Ca), (b) ZAM1100(1Ca), and (c) ZXAM2100 (1Ca) samples. The red rectangular region indicates the position where the EDS elemental maps were obtained, and the results are shown in Fig. 8 (d–h). As indicated by the red arrows, the ZXAM1100(1Ca) sample contained numerous fine particles measuring ~1 μm in diameter. By contrast, fine particles were not observed in the ZXAM2100(0.5Ca) and ZXAM2100(1Ca) samples. The fine particles in the ZXAM1100(1Ca) sample were enriched with Ca, thus indicating the formation of a Mg_2Ca phase.

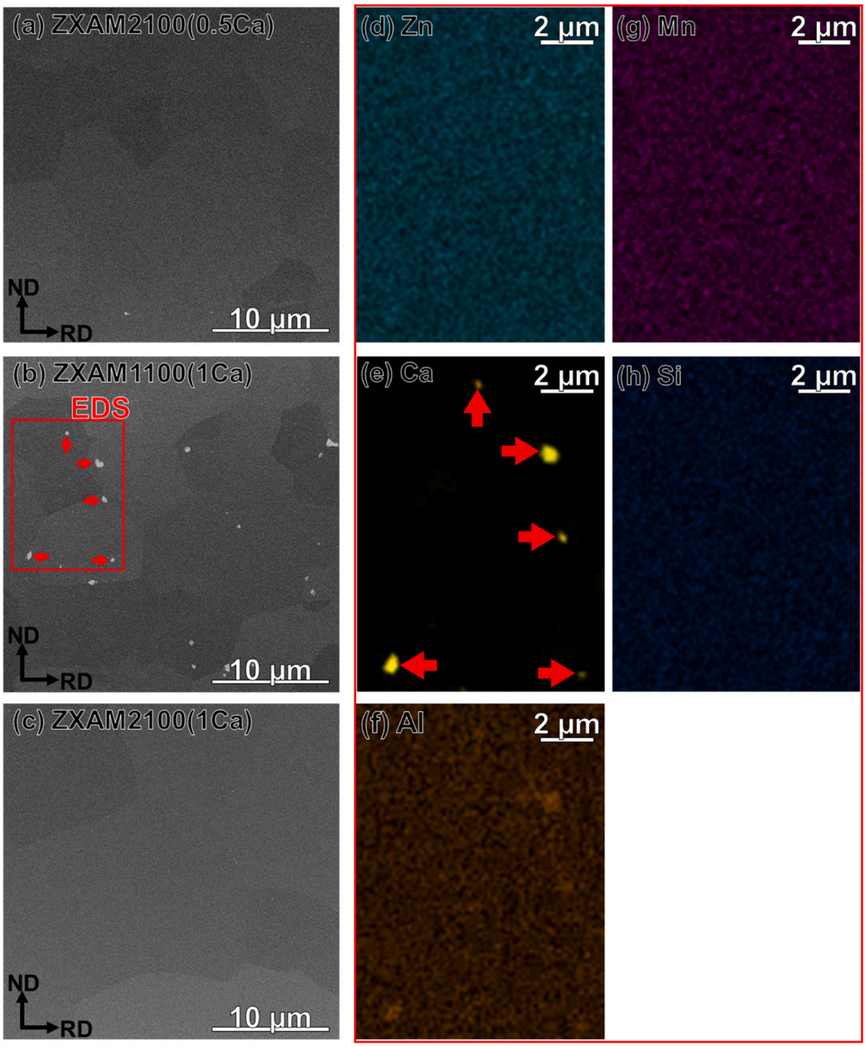

Fig. 8. Magnified BSE images of solution-treated (a) ZXAM2100(0.5Ca), (b) ZXAM1100(1Ca), and (c) ZXAM2100(1Ca) samples. EDS elemental maps obtained from red rectangle in Fig. 8 (b) are shown in Fig. 8 (d–h).

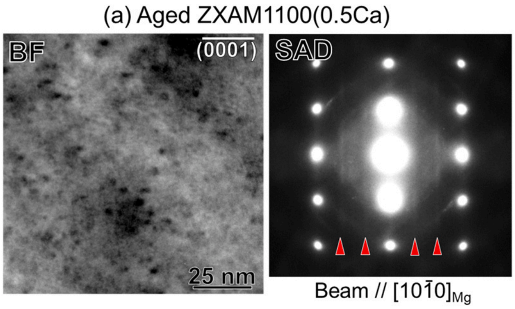
(a) Aged ZXAM1100(0.5Ca)

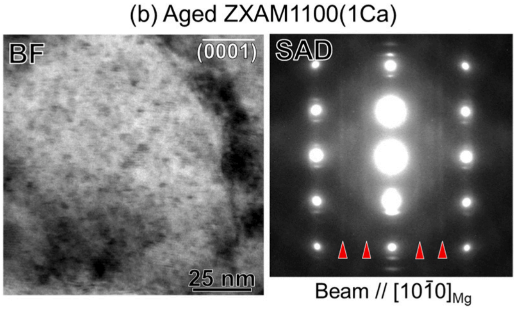
(b) Aged ZXAM1100(1Ca)

Fig. 9. Bright-field (BF) TEM images and selected area diffraction (SAD) patterns of aged (a) ZXAM1100(0.5Ca) and (b) ZXAM1100(1Ca) samples.

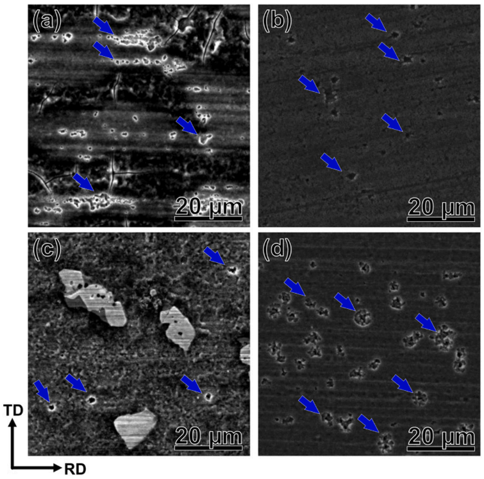

Fig. 10. Secondary electron SEM images of solution-treated (a) ZXAM2000 (0.2Ca), (b) ZXAM2100(0.5Ca), (c) ZXAM2100(1Ca), and (d) aged ZXAM2100 (0.5Ca) samples after 1-hour immersion test. Blue arrows indicate corrosion pits.

Fig. 9 shows the bright-field (BF) TEM images and selected area diffraction (SAD) patterns of the aged (a) ZXAM1100(0.5Ca) and (b) ZXAM1100(1Ca) samples obtained from the [10$\bar{1}$0] direction. Speckled contrasts were observed along the (0001) planes in the BF images. Furthermore, continuous and faint streaks were observed along the [0001] direction at 1/3(11$\bar{2}$0) and 2/3(11$\bar{2}$0) in the SAD patterns, as indicated by the red arrowheads. Such features indicate that the aging-treatment formed Guinier-Preston (G.P.) zones [20–23].

Fig. 10 shows the SEM images of the solution-treated (a) ZXAM2000 (0.2Ca), (b) ZXAM2100(0.5Ca), (c) ZXAM2100(1Ca), and (d) aged ZXAM2100(0.5Ca) samples after immersion for 1 hour. All the samples showed corrosion pits, as indicated by the blue arrows. The pits on the solution-treated ZXAM2000(0.2Ca) sample were larger than those on the other samples. In fact, the aged ZXAM2100(0.5Ca) sample exhibited a relatively high density of corrosion pits.

Fig. 11 shows the high-magnification SEM images of the solution-treated (a) ZXAM2000(0.2Ca), (b) ZXAM2100(0.5Ca), (c) ZXAM2100 (1Ca), and (d) aged ZXAM2100(0.5Ca) samples after immersion for 12 hours. Needle-shaped corrosion products were observed. The corrosion products on both the solution-treated and aged ≥ 0.5 %Ca-containing samples were dense, whereas the solution-treated ZXAM2000 (0.2Ca) and ZXAM2100(1Ca) samples showed a relatively sparse distribution of the corrosion products. In particular, the solution-treated ZXAM2000(0.2Ca) sample showed the coarsest corrosion products among all the samples.

4. Discussion

In this work, we investigated the effects of Zn and Ca contents on the age-hardening responses, room-temperature (RT) formability, tensile properties, and corrosion properties of Mg-Zn-Ca-Al-Mn (ZXAM) alloy sheets.

Fig. 12(a) shows the relationship between the PS along the RD and the I.E. values of various Mg and Al alloy sheets [4,6,7,13–16,20, 34–56]. The relationship between the PS along the RD (or the extrusion direction for extruded samples) and the corrosion rate obtained by a 3.5mass%NaCl immersion test of various wrought Mg alloys is shown in Fig. 12(b) [9,17,19,44,57–62]. The PS of the Mg alloys decreased as the I.E. value and corrosion rate improved, as indicated by the gray area. By contrast, our ZXAM2100(0.5Ca) sheet simultaneously overcame the trade-off relationship, as evidenced by an I.E. value of 8.7 mm after the solution-treatment and a high PS of 213 MPa along the RD after the aging-treatment. These properties are comparable to those of recently developed low-cost and RT-formable Mg alloys [14,15,42]. Moreover, the aged ZXAM2100(0.5Ca) sheet indicated a low corrosion rate of 3.0 $\mathrm{mm \cdot y^{-1}}$, which is ~2/5 lower than that of a ZXAM alloy with a moderate Mn content of 0.5mass% (corrosion rate: 7.0 $\mathrm{mm \cdot y^{-1}}$) [17]. This indicates that age-hardening is an effective method for achieving an excellent balance among strength, RT formability, and corrosion resistance.

The I.E. value was significantly increased to 8–9 mm by the 0.5 %Ca addition, and the solution-treated 0.5 %Ca-containing sheets indicated good EFs of ~23 % and ~30 % for the RD and TD, respectively. This is attributed to the relatively fine grain structure with TD-split textural features. The yield plateau in the ≥ 0.5 %Ca-containing sheets would result from the formation and propagation of tensile twinning because the addition of ≥ 0.5 %Ca resulted in a tilting of the (0001) poles toward the RD and TD, which facilitates the deformation by tensile twinning [45,63]. Moreover, the tilting of the (0001) poles toward the TD was relatively large (Fig. 3). This would enhance the activation of tensile twinning during the TD-tension, resulting in a relatively large plateau region.

The 0.5 %Ca-containing sheets maintained their favorable EFs even after the aging-treatment, as reported in previous studies [20,43,64,65]. Although the textural features of the 1 %Ca-containing sheets were nearly identical to those of the 0.5 %Ca-containing sheets, both the solution-treated and aged 1 %Ca-containing sheets showed the I.E. values of ~6 mm and EFs of ~20 % for both the RD and TD. The decrease in the I.E. values and EFs was due to the coarse particles aligning with the RD (Fig. 7(c) and (d)), as they would act as initiation sites for cracks during plastic deformation [66]. In particular, these particles may significantly decrease the EF along the TD [67].

Except for the case of the 0.2 %Ca-containing sheets, the 2 %Zn addition led to an increase in the I.E. values (Fig. 4), presumably due to the improvement in the work-hardening capacity by the solid-solution of Zn [34]. The 0.2 %Ca-containing sheets showed isotropic and strong basal texture features, resulting in poor RT formability with the I.E. values of ~3 mm and in-plane isotropy. In general, the trace addition of Ca (0.1mass%) to Mg-Zn alloys can result in a TD-split texture [49] owing to the grain boundary segregation of Zn and Ca [43,68,69]. However, Ca combined with Si (an impurity), forms the MgSiCa phase (Fig. 7(a)) [70,71]. Therefore, the segregation of Ca along the grain

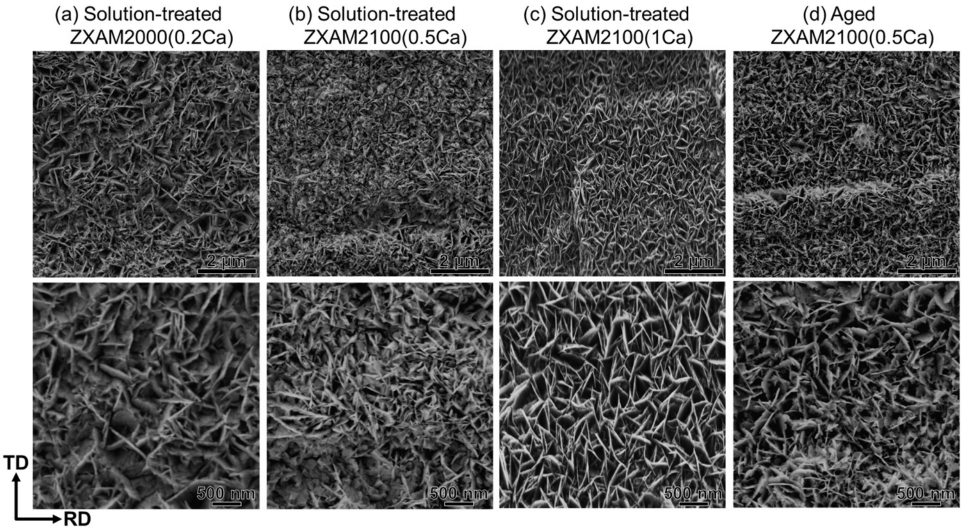

Fig. 11. Secondary electron SEM images of solution-treated (a) ZXAM2000(0.2Ca), (b) ZXAM2100(0.5Ca), (c) ZXAM2100(1Ca), and (d) aged ZXAM2100(0.5Ca) samples after 12-hours immersion test.

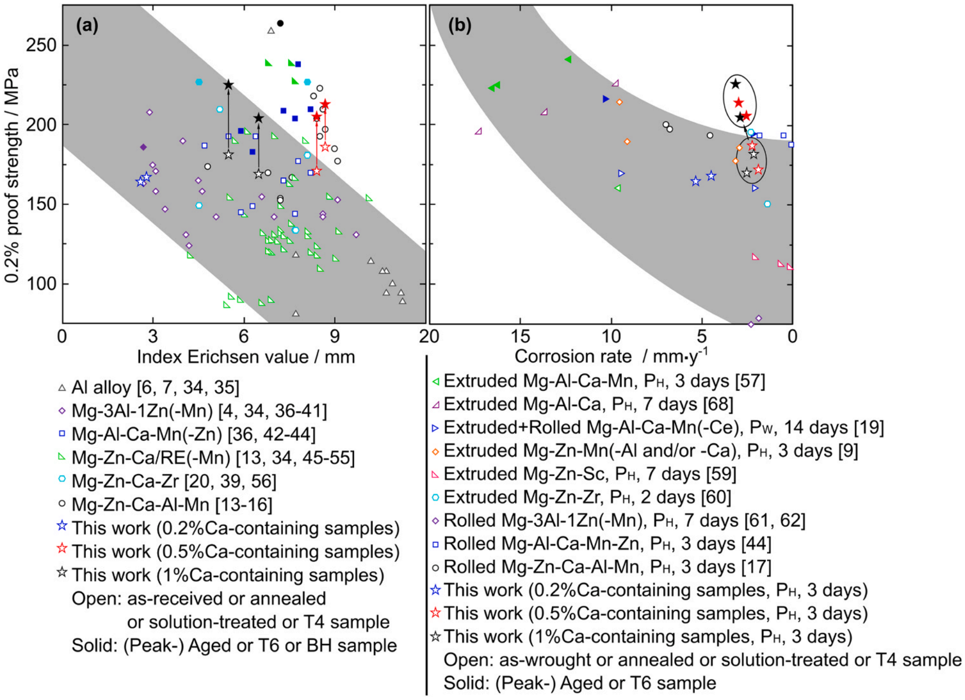

Fig. 12. Relationships between (a) 0.2 % proof strength (PS) and Index Erichsen values for various Mg and Al alloy sheets; (b) PS along the RD (or extrusion direction) and corrosion rate in 3.5mass% NaCl solution of various wrought Mg alloys. Corrosion rates obtained using weight-loss and hydrogen-evolution methods are denoted as P_W and P_H, respectively. Immersion time is shown in Fig. 12 (b).

boundaries is reduced, thus limiting the textural changes in this work.

The solution-treated ZXAM1100(0.5Ca) sheet exhibited moderate PSs of 171 and 130 MPa for the RD and TD, respectively. The PSs increased slightly after the 2 %Zn addition, and the PSs of the solution-treated ZXAM2100(0.5Ca) sheet were 186 and 139 MPa for the RD and TD, respectively. This is attributable to the relatively fine grain size of the ZXAM2100(0.5Ca) sheet (Fig. 6). The PSs of the solution-treated ZXAM2100(0.5Ca) sheet were slightly lower than those of the other ZXAM sheets, presumably owing to the decrease in the density of the Al-Mn pinning precipitates and the resulting grain coarsening. [15,17].

However, our alloy sheets formed G.P. zones after aging (Fig. 9), and the PSs of the aged ZXAM2100(0.5Ca) sheet increased to 213 and 164 MPa along the RD and TD, respectively. Fig. 13 summarizes the mechanism models for achieving favorable RT formability and high strength. The PSs were comparable to those of recently developed high-Mn-containing Mg-3Zn-0.5Ca-0.5Al-1Mn sheets (223 and 157 MPa along the RD and TD, respectively) [15]. The PSs of the solution-treated sheets were further increased by adding 1 %Ca when the Zn content was 1 %. The improved PS along the TD of the ZXAM1100(1Ca) sheet contributed to the relatively small anisotropy of the PS (PS_{TD}/PS_{RD}) compared with that of the 0.5 %Ca-containing sheets. This could be due to the suppression of the occurrence and propagation of twinning through the fine grain structure and dispersion of fine Mg_2Ca particles in the ZXAM1100(1Ca) sheet (Fig. 8) [72–75]. The 1 %Ca addition to the

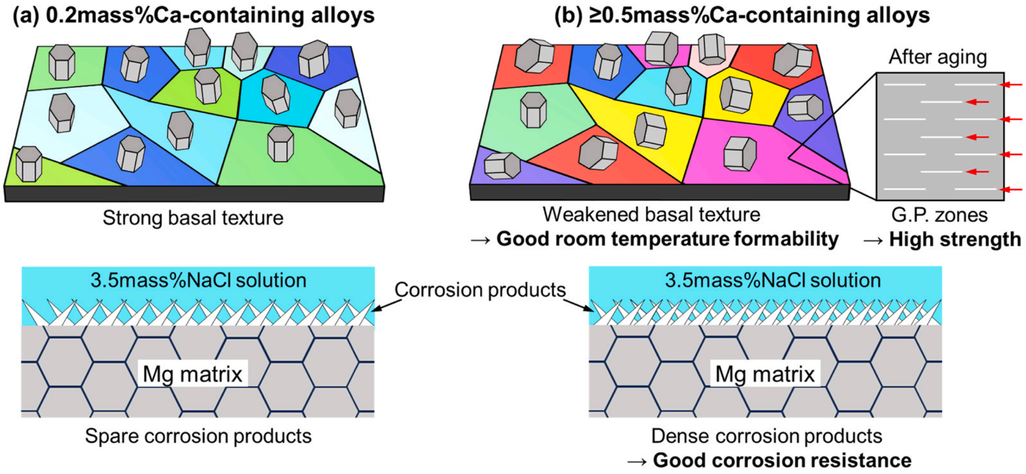

Fig. 13. Schematic showing mechanism models for simultaneously achieving an excellent combination of RT formability, strength, and corrosion resistance: (a) 0.2 %Ca-containing and (b) ≥ 0.5 %Ca-containing samples.

2 %Zn-containing sheets resulted in grain coarsening and reduced the PSs. A $Ca_2Mg_6Zn_3$ phase was formed in this alloy sheet at the expense of the Mg_2Ca phase. The $Ca_2Mg_6Zn_3$ phase exhibited limited thermal stability [32,66], and the particles would be dissolved in the Mg matrix during the solution-treatment. Therefore, the grain boundary pinning effect weakened, thus resulting in grain coarsening. This suggests that the $Ca_2Mg_6Zn_3$ phase is not suitable for the development of heat-treatable wrought Mg alloys because grain coarsening occurs during solution-treatment at high temperatures. In the 0.2 %Ca-containing sheets, an increase in the Zn content from 1 % to 2 % improved the anisotropy of the PS ($PS_{TD}/PS_{RD} = 1$). This may result from a decrease in the critical resolved shear stress of the prismatic slip [76]. The 2 % Zn-containing sheets exhibited higher UTSs than the 1 %Zn-contaning sheets because of solid-solution strengthening by Zn.

The corrosion rate was slightly improved by ~1 $mm \cdot y^{-1}$ by the 2 % Zn addition in the 0.2 %Ca-containing alloys, presumably owing to an increase in the corrosion potential by the solid-solution of Zn [77]. By contrast, the ≥ 0.5 %Ca addition significantly improved the corrosion rate to 2.0–2.5 $mm \cdot y^{-1}$ in the solution-treated state. The corrosion resistance is affected by galvanic corrosion between the particles and Mg matrix [17,19,78–81], the textural features [82–85], the grain size [79,84,86–88], and the density of the corrosion products [18,19,44]. The particle distribution and grain size of the solution-treated ZXAM2100 (0.5Ca) sheet were nearly identical to those of the ZXAM2000(0.2Ca) sheet [89]. Moreover, the ≥ 0.5 %Ca addition weakened the basal texture feature (Fig. 6), which generally promotes corrosion [82–85]. Therefore, the significantly improved corrosion resistance owing to the ≥ 0.5 %Ca addition can be interpreted by the dense corrosion products, which prevent the contact of NaCl water with the metal surface [90]. The ≥ 0.5 %Ca-containing sheets were covered with dense corrosion products after 12 hours immersion (Fig. 11). Fig. 13 shows a schematic diagram of 0.2 %Ca- and ≥ 0.5 %Ca-containing alloys during the immersion test, which visually illustrates the key factors for the corrosion resistance. The 1 %Ca addition slightly increased the corrosion rate by 0.2–0.3 $mm \cdot y^{-1}$, presumably owing to the significant number of particles. The aging led to 0.5–1.0 $mm \cdot y^{-1}$ faster corrosion rates than those of the solution-treated state; the corrosion rate of the aged ZXAM2100 (0.5Ca) sheet was 3.0 $mm \cdot y^{-1}$. This is attributable to the G.P. zones [57], as confirmed by the relatively high density of corrosion pits after 1 hour immersion of the aged sample (Fig. 10). However, the decrease in the corrosion resistance was limited [19,57].

5. Conclusion

The effects of Zn and Ca contents on the room-temperature formability, tensile properties, and corrosion properties of an age-hardenable Mg-Zn-Ca-Al-Mn alloy sheet with low Mn content were investigated. The Ca content significantly improved the formability, strength, and corrosion resistance, and the Mg-2Zn-0.5Ca-0.2Al-0.2Mn (mass%) alloy exhibited an excellent combination of formability, strength, and corrosion resistance after age-hardening. For practical automotive applications, corrosion resistance is a crucial factor in addition to strength and formability; therefore, the developed alloy sheet is a promising candidate for automotive applications and contributes to a significant reduction in greenhouse gas emissions. The main conclusions are as follows:

1. The increase in Zn content increased the ultimate tensile strength and Index Erichsen value, presumably owing to the solid-solution of Zn.
2. The addition of more than 0.5mass%Ca led to a texture with the inclination of the (0001) poles toward the transverse direction whereas the 0.2mass%Ca-containing alloys exhibited a strong basal texture with the (0001) poles aligned to the normal direction. Such weakened texture features significantly improved the Index Erichsen value.
3. The age-hardening response was improved by the addition of ≥ 0.5mass%Ca owing to the formation of G.P. zones. Consequently, the 0.2 % proof strengths of the ≥ 0.5mass%Ca-containing alloy sheets were increased by 30–40 MPa for both the rolling and transverse directions
4. The excess addition of 1mass%Ca formed large particles with a diameter of 10–15 μm, thus resulting in a decrease in the Index Erichsen value and ductility.
5. The addition of 0.5mass%Ca resulted in the formation of dense corrosion products. Consequently, the corrosion resistance was significantly improved. Although aging decreased the corrosion resistance only slightly, it remained higher than those of commercial Mg alloys.

CRediT authorship contribution statement

Taisuke Sasaki: Writing – review & editing, Resources, Funding acquisition. **Zehao Li:** Writing – review & editing, Investigation. **Shigeharu Kamado:** Writing – review & editing, Project administration, Funding acquisition. **Yukio Miyashita:** Writing – review & editing, Supervision. **Kaito Kikuchi:** Writing – original draft, Validation, Investigation, Conceptualization. **Taiki Nakata:** Writing – review & editing, Resources, Methodology, Funding acquisition.

Declaration of Competing Interest

The authors declare that they have no known competing financial interests or personal relationships that could have appeared to influence the work reported in this paper.

Acknowledgements

The authors thank Luo Xuan (Nanjing Tech University, China) for valuable discussions. This work was supported by JSPS KAKENHI Grant Numbers JP22H00259, JP24K01213, JP23K17833, Osawa Scientific Studies Grants Foundation, Japan, and The Light Metal Educational Foundation, Inc., Japan. The authors would also like to thank Editage (www.editage.com) for English language editing.

Data Availability

All data are available from the corresponding author on reasonable request.

References

[1] B. Liu, J. Yang, X. Zhang, Q. Yang, J. Zhang, X. Li, Development and application of magnesium alloy parts for automotive OEMs: a review, J. Magnes. Alloy. 11 (2023) 15–47, https://doi.org/10.1016/J.JMA.2022.12.015.

[2] T.T. Sasaki, M.-Z. Bian, Z.H. Li, K. Hono, Toward development of strong and formable magnesium alloy sheets with bake-hardenability, JOM 73 (2021) 1471–1483, https://doi.org/10.1007/s11837-021-04613-1.

[3] A.A. Luo, R. Shi, J. Miao, T. Avey, Review: magnesium sheet alloy development for room temperature forming, JOM 73 (2021) 1403–1418, https://doi.org/10.1007/s11837-021-04616-y.

[4] X. Huang, K. Suzuki, Y. Chino, M. Mabuchi, Improvement of stretch formability of Mg–3Al–1Zn alloy sheet by high temperature rolling at finishing pass, J. Alloy. Compd. 509 (2011) 7579–7584, https://doi.org/10.1016/J.JALLCOM.2011.04.132.

[5] T. Nakata, C. Xu, H. Ohashi, Y. Yoshida, K. Yoshida, S. Kamado, New Mg–Al based alloy sheet with good room-temperature stretch formability and tensile properties, Scr. Mater. 180 (2020) 16–22, https://doi.org/10.1016/j.scriptamat.2020.01.015.

[6] S.M. Hirth, G.J. Marshall, S.A. Court, D.J. Lloyd, Effects of Si on the aging behaviour and formability of aluminium alloys based on AA6016, Mater. Sci. Eng. A 319– 321 (2001) 452–456, https://doi.org/10.1016/S0921-5093(01)00969-8.

[7] S.A. Court, K.M. Gatenby, D.J. Lloyd, Factors affecting the strength and formability of alloys based on Al-3 wt% Mg, Mater. Sci. Eng. A 319–321 (2001) 443–447, https://doi.org/10.1016/S0921-5093(00)02018-9.

[8] M. Bian, X. Huang, Y. Chino, Substantial improvement in cold formability of concentrated Mg–Al–Zn–Ca alloy sheets by high temperature final rolling, Acta Mater. 220 (2021) 117328, https://doi.org/10.1016/J.ACTAMAT.2021.117328.

[9] T. Nakata, C. Xu, H. Yamato, L. Geng, S. Kamado, Effect of microalloyed Al and Ca on mechanical properties and corrosion resistance of high-speed extruded Mg-2Zn-1Mn (mass%) alloy, Mater. Charact. 191 (2022) 112121, https://doi.org/10.1016/J.MATCHAR.2022.112121.

[10] T.S. Wang, Z.M. Hua, C. Wang, M. Zha, Y. Gao, H.Y. Wang, Realizing impressive superplasticity in a low-alloyed Mg-Zn-Ca-Al-Mn alloy: the roles of grain boundary segregation and dense β-Mn particles, J. Magnes. Alloy. 12 (2024) 4085–4095, https://doi.org/10.1016/J.JMA.2023.05.014.

[11] Y.L. Ying, Z.P. Guan, X. Wang, G. Wang, W. Yan, Creep behaviors of Mg–6Zn-0.4Mn-0.3Al-0.2Ca (wt%) alloy enhanced by icosahedral quasicrystal, Mater. Sci. Eng.: A 892 (2024) 146060, https://doi.org/10.1016/J.MSEA.2023.146060.

[12] H. Yeganeh, A. Bahmani, M. Lotfpour, M. Malekan, M. Emamy, B. Nayebi, K. S. Shin, Enhanced oxidation and overheating resistance of the extruded Mg–Zn–Al–Mn magnesium alloy by Calcium addition, J. Magnes. Alloy. 11 (2023) 1276–1291, https://doi.org/10.1016/J.JMA.2023.03.004.

[13] T. Nakata, C. Xu, S. Kamado, Improving tensile properties of a room-temperature formable and heat-treatable Mg–6Zn-0.2Ca (wt%) alloy sheet via micro-alloying of Al and Mn, Mater. Sci. Eng. A 772 (2020) 138690, https://doi.org/10.1016/j.msea.2019.138690.

[14] X. Huang, M. Bian, I. Nakatsugawa, Y. Chino, M. Sato, K. Yamazaki, F. Kido, H. Ueda, M. Inoue, Influence of aluminum content on microstructure and performance of Mg-Zn-Ca-Al-Mn magnesium alloys, J. Alloy. Compd. 948 (2023) 169719, https://doi.org/10.1016/J.JALLCOM.2023.169719.

[15] X. Huang, M. Bian, I. Nakatsugawa, Y. Chino, M. Sato, K. Yamazaki, F. Kido, H. Ueda, M. Inoue, Simultaneously achieving excellent mechanical properties and high thermal conductivity in a high Mn-containing Mg-Zn-Ca-Al-Mn sheet alloy, J. Alloy. Compd. 887 (2021) 161394, https://doi.org/10.1016/j.jallcom.2021.161394.

[16] J.K. Lee, H.S. Jang, A. Zargaran, A.J.S.F. Tapia, N.J. Kim, B.J. Lee, A thermodynamic approach to the precipitation hardening of magnesium alloy with high formability, Scr. Mater. 226 (2023) 115231, https://doi.org/10.1016/J.SCRIPTAMAT.2022.115231.

[17] B.Y. Wang, M.X. Li, Y.J. Li, Y.F. Wang, Y. Gao, H.Y. Wang, Effect of Al/Mn ratio on corrosion behavior of lean Mg-Zn-Ca-Al-Mn alloy processed by twin-roll casting, Corros. Sci. 212 (2023) 110938, https://doi.org/10.1016/J.CORSCI.2022.110938.

[18] X. Zhang, D. Wang, F. Cao, C. Wang, M.X. Li, Y. Yang, M. Zha, Negatively correlated corrosion and stress corrosion cracking of Mg-Al-Mn-Ca based alloys, Corros. Sci. 227 (2024) 111747, https://doi.org/10.1016/J.CORSCI.2023.111747.

[19] J.S. Li, M.X. Li, Z.M. Hua, Y.T. Mo, K. Guan, M. Zha, Y. Gao, H.Y. Wang, A corrosion-resistant and age-hardenable Mg-Al-Mn-Ca-Ce dilute alloy with fine-grained structure processed by controlled rolling, J. Mater. Sci. Technol. 163 (2023) 223–236, https://doi.org/10.1016/J.JMST.2023.04.029.

[20] Z.H. Li, T.T. Sasaki, T. Shiroyama, A. Miura, K. Uchida, K. Hono, Simultaneous achievement of high thermal conductivity, high strength and formability in Mg-Zn-Ca-Zr sheet alloy, Mater. Res Lett. 8 (2020) 335–340, https://doi.org/10.1080/21663831.2020.1759718.

[21] Z.H. Li, T.T. Sasaki, A. Uedono, K. Hono, Role of Zn on the rapid age-hardening in Mg-Ca-Zn alloys, Scr. Mater. 216 (2022) 114735, https://doi.org/10.1016/J.SCRIPTAMAT.2022.114735.

[22] K. Oh-ishi, R. Watanabe, C.L. Mendis, K. Hono, Age-hardening response of Mg–0.3 at%Ca alloys with different Zn contents, Mater. Sci. Eng.: A 526 (2009) 177–184, https://doi.org/10.1016/J.MSEA.2009.07.027.

[23] X. Gao, S.M. Zhu, B.C. Muddle, J.F. Nie, Precipitation-hardened Mg–Ca–Zn alloys with superior creep resistance, Scr. Mater. 53 (2005) 1321–1326, https://doi.org/10.1016/J.SCRIPTAMAT.2005.08.035.

[24] G. Song, A. Atrens, Understanding magnesium corrosion. A framework for improved alloy performance, Adv. Eng. Mater. 5 (2003) 837–858, https://doi.org/10.1002/adem.200310405.

[25] C. Zhang, L. Wu, G. Huang, Y. Huang, B. Jiang, A. Atrens, F. Pan, Effect of microalloyed Ca on the microstructure and corrosion behavior of extruded Mg alloy AZ31, J. Alloy. Compd. 823 (2020) 153844, https://doi.org/10.1016/J.JALLCOM.2020.153844.

[26] C. Liu, X. Chen, J. Chen, A. Atrens, F. Pan, The effects of Ca and Mn on the microstructure, texture and mechanical properties of Mg-4 Zn alloy, J. Magnes. Alloy. 9 (2021) 1084–1097, https://doi.org/10.1016/J.JMA.2020.03.012.

[27] Z. Zareian, M. Emamy, M. Malekan, H. Mirzadeh, W.J. Kim, A. Bahmani, Tailoring the mechanical properties of Mg–Zn magnesium alloy by calcium addition and hot extrusion process, Mater. Sci. Eng.: A 774 (2020) 138929, https://doi.org/10.1016/J.MSEA.2020.138929.

[28] H. Li, E. Hsu, J. Szpunar, H. Utsunomiya, T. Sakai, Deformation mechanism and texture and microstructure evolution during high-speed rolling of AZ31B Mg sheets, J. Mater. Sci. 43 (2008) 7148–7156, https://doi.org/10.1007/s10853-008-3021-3.

[29] J. Gröbner, I. Chumak, R. Schmid-Fetzer, Experimental study of ternary Ca–Mg–Si phase equilibria and thermodynamic assessment of Ca–Si and Ca–Mg–Si systems, Intermetallics 11 (2003) 1065–1074, https://doi.org/10.1016/J.INTERMET.2003.07.001.

[30] P. VillarsPearson's, handbook desk edition crystallographic data for intermetallic phases, 1, ASM International, Materials Park, OH, 1997 (n.d.).

[31] J.F. Nie, B.C. Muddle, Precipitation hardening of Mg-Ca(-Zn) alloys, Scr. Mater. 37 (1997) 1475–1481, https://doi.org/10.1016/S1359-6462(97)00294-7.

[32] P.M. Jardim, G. Solórzano, J.B.V. Sande, Second phase formation in melt-spun Mg–Ca–Zn alloys, Mater. Sci. Eng.: A 381 (2004) 196–205, https://doi.org/10.1016/J.MSEA.2004.04.043.

[33] C.O. Brubaker, Z.K. Liu, A computational thermodynamic model of the Ca–Mg–Zn system, J. Alloy. Compd. 370 (2004) 114–122, https://doi.org/10.1016/J.JALLCOM.2003.08.097.

[34] D.H. Kang, D.W. Kim, S. Kim, G.T. Bae, K.H. Kim, N.J. Kim, Relationship between stretch formability and work-hardening capacity of twin-roll cast Mg alloys at room temperature, Scr. Mater. 61 (2009) 768–771, https://doi.org/10.1016/J.SCRIPTAMAT.2009.06.026.

[35] F. Ozturk, E. Esener, S. Toros, C.R. Picu, Effects of aging parameters on formability of 6061-O alloy, Mater. Des. 31 (2010) 4847–4852, https://doi.org/10.1016/J.MATDES.2010.05.050.

[36] M.Z. Bian, T.T. Sasaki, T. Nakata, Y. Yoshida, N. Kawabe, S. Kamado, K. Hono, Bake-hardenable Mg–Al–Zn–Mn–Ca sheet alloy processed by twin-roll casting, Acta Mater. 158 (2018) 278–288, https://doi.org/10.1016/j.actamat.2018.07.057.

[37] T. Nakata, Z.H. Li, T.T. Sasaki, K. Hono, S. Kamado, Role of grain boundary segregation on microstructural development in basal-textured Mg-Al-Zn alloy sheet, Scr. Mater. 218 (2022) 114828, https://doi.org/10.1016/J.SCRIPTAMAT.2022.114828.

[38] X. Huang, K. Suzuki, Y. Chino, Influences of initial texture on microstructure and stretch formability of Mg–3Al–1Zn alloy sheet obtained by a combination of high temperature and subsequent warm rolling, Scr. Mater. 63 (2010) 395–398, https://doi.org/10.1016/J.SCRIPTAMAT.2010.04.032.

[39] M.Z. Bian, Z.R. Zeng, S.W. Xu, S.M. Zhu, Y.M. Zhu, C.H.J. Davies, N. Birbilis, J. F. Nie, Improving Formability of Mg–Ca–Zr Sheet Alloy by Microalloying of Zn, Adv. Eng. Mater. 18 (2016) 1763–1769, https://doi.org/10.1002/adem.201600293.

[40] H. Zhang, W. Cheng, J. Fan, B. Xu, H. Dong, Improved mechanical properties of AZ31 magnesium alloy sheets by repeated cold rolling and annealing using a small pass reduction, Mater. Sci. Eng.: A 637 (2015) 243–250, https://doi.org/10.1016/J.MSEA.2015.04.057.

[41] T. Nakata, T. Matsuno, R. Oki, S. Kamado, Effect of micro-texture on tensile properties and room-temperature stretch formability of Mg-Al-Zn alloy sheet, J. Alloy. Compd. 938 (2023) 168519, https://doi.org/10.1016/J.JALLCOM.2022.168519.

[42] M.Z. Bian, T.T. Sasaki, B.C. Suh, T. Nakata, S. Kamado, K. Hono, A heat-treatable Mg–Al–Ca–Mn–Zn sheet alloy with good room temperature formability, Scr. Mater. 138 (2017) 151–155, https://doi.org/10.1016/j.scriptamat.2017.05.034.

[43] Z.H. Li, T.T. Sasaki, M.Z. Bian, T. Nakata, Y. Yoshida, N. Kawabe, S. Kamado, K. Hono, Role of Zn on the room temperature formability and strength in Mg–Al–Ca–Mn sheet alloys, J. Alloy. Compd. 847 (2020) 1–11, https://doi.org/10.1016/j.jallcom.2020.156347.

[44] T. Nakata, C. Xu, N.A.S. binti Osman, L. Geng, S. Kamado, Development of corrosion-resistant Mg-Al-Ca-Mn-Zn alloy sheet with good tensile properties and stretch formability, J. Alloy. Compd. 910 (2022) 164752, https://doi.org/10.1016/J.JALLCOM.2022.164752.

[45] T. Nakata, T. Hama, K. Sugiya, S. Kamado, Understanding room-temperature deformation behavior in a dilute Mg–1.52Zn–0.09Ca (mass%) alloy sheet with weak basal texture, Mater. Sci. Eng.: A 852 (2022) 143638, https://doi.org/10.1016/J.MSEA.2022.143638.

[46] M. Yuasa, N. Miyazawa, M. Hayashi, M. Mabuchi, Y. Chino, Effects of group II elements on the cold stretch formability of Mg–Zn alloys, Acta Mater. 83 (2015) 294–303, https://doi.org/10.1016/J.ACTAMAT.2014.10.005.

[47] Y. Chino, K. Sassa, X. Huang, K. Suzuki, M. Mabuchi, Effects of zinc concentration on the stretch formability at room temperature of the rolled Mg-Zn-Ca alloys, Nippon Kinzoku Gakkaishi J. Jpn. Inst. Met 75 (2011) 35–41, https://doi.org/10.2320/jinstmet.75.35.

[48] D.W. Kim, B.C. Suh, M.S. Shim, J.H. Bae, D.H. Kim, N.J. Kim, Texture evolution in Mg-Zn-Ca alloy sheets, in: Metall Mater Trans A Phys Metall Mater Sci, Springer, Boston, 2013, pp. 2950–2961, https://doi.org/10.1007/s11661-013-1674-2.

[49] Y. Chino, X. Huang, K. Suzuki, M. Mabuchi, Enhancement of stretch formability at room temperature by addition of Ca in Mg-Zn alloy, Mater. Trans. 51 (2010) 818–821, https://doi.org/10.2320/matertrans.M2009385.

[50] M. Zhou, X. Huang, Y. Morisada, H. Fujii, Y. Chino, Effects of Ca and Sr additions on microstructure, mechanical properties, and ignition temperature of hot-rolled Mg–Zn alloy, Mater. Sci. Eng.: A 769 (2020) 138474, https://doi.org/10.1016/J.MSEA.2019.138474.

[51] W. xue Fan, Y. Bai, G. yang Li, X. yang Chang, H. Hao, Enhanced mechanical properties and formability of hot-rolled Mg–Zn–Mn alloy by Ca and Sm alloying, Trans. Nonferrous Met. Soc. China 32 (2022) 1119–1132, https://doi.org/10.1016/S1003-6326(22)65860-6.

[52] T. Nakata, Z.H. Li, T.T. Sasaki, K. Hono, S. Kamado, Room-temperature stretch formability, tensile properties, and microstructures of precipitation hardenable Mg–6Zn-0.2Ca (mass%) alloy sheets micro-alloyed with Ce or Y, Mater. Sci. Eng.: A 804 (2021) 140563, https://doi.org/10.1016/J.MSEA.2020.140563.

[53] Y. Chino, X. Huang, K. Suzuki, K. Sassa, M. Mabuchi, Influence of Zn concentration on stretch formability at room temperature of Mg–Zn–Ce alloy, Mater. Sci. Eng.: A 528 (2010) 566–572, https://doi.org/10.1016/J.MSEA.2010.09.081.

[54] M. Bian, X. Huang, M. Mabuchi, Y. Chino, Compositional optimization of Mg–Zn–Sc sheet alloys for enhanced room temperature stretch formability, J. Alloy. Compd. 818 (2020) 152891, https://doi.org/10.1016/J.JALLCOM.2019.152891.

[55] Y. Matsuoka, M. Bian, X. Huang, Y. Tsukada, T. Koyama, Y. Chino, Simulation-aided analysis on mechanical properties of dilute Mg-Zn-Ca alloy sheets, J. Alloy. Compd. 906 (2022) 164285, https://doi.org/10.1016/J.JALLCOM.2022.164285.

[56] T. Bhattacharjee, B.C. Suh, T.T. Sasaki, T. Ohkubo, N.J. Kim, K. Hono, High strength and formable Mg–6.2Zn–0.5Zr–0.2Ca alloy sheet processed by twin roll casting, Mater. Sci. Eng.: A 609 (2014) 154–160, https://doi.org/10.1016/J.MSEA.2014.04.058.

[57] K. Zhang, C. Wang, D.W. Wang, M.X. Li, Y.L. Ma, Z.M. Hua, L.Y. Zhang, J. Li, H. Y. Wang, Effects of solute redistribution during heat treatment on micro-galvanic corrosion behavior of dilute Mg-Al-Ca-Mn alloy, Corros. Sci. 213 (2023) 110971, https://doi.org/10.1016/J.CORSCI.2023.110971.

[58] Z. Fu, Z. Wang, G. Li, Y. Yao, H. Yu, Y. Liu, T. Zheng, H. Xiong, Microstructure, mechanical and corrosion properties of Mg-1.61Al-1.76Ca alloy under different extrusion temperatures, J. Mater. Eng. Perform. 29 (2020) 672–680, https://doi.org/10.1007/s11665-020-04557-8.

[59] W. Ci, X. Chen, Y. Sun, X. Dai, G. Zhu, D. Zhao, F. Pan, Effect of Zn on mechanical and corrosion properties of Mg-Sc-Zn alloys, J. Mater. Sci. Technol. 158 (2023) 31–42, https://doi.org/10.1016/J.JMST.2023.01.058.

[60] B.J. Wang, D.K. Xu, J. Sun, E.H. Han, Effect of grain structure on the stress corrosion cracking (SCC) behavior of an as-extruded Mg-Zn-Zr alloy, Corros. Sci. 157 (2019) 347–356, https://doi.org/10.1016/J.CORSCI.2019.06.017.

[61] L. Wang, Y. Lu, H. Chai, G. Huang, X. Fu, X. Cao, H. Zhang, H. Wang, M. Vedani, Effect of residual tensile stress and crystallographic structure on corrosion behavior of AZ31 Mg alloy rolled sheets, Mater. Today Commun. 32 (2022) 104065, https://doi.org/10.1016/J.MTCOMM.2022.104065.

[62] T. Han, L. Wang, Y. Lu, L. Lu, H.R. Tiyyagura, Effect of tensile direction on corrosion behavior of AZ31 magnesium alloy rolled sheets, J. Mater. Eng. Perform. (2023), https://doi.org/10.1007/s11665-023-08558-1.

[63] T. Hama, T. Nakata, K. Higuchi, H. Yoshida, Y. Jono, Plastic deformation behavior of a Mg-1.5Zn-0.1Ca (mass%) alloy sheet under different strain paths, Mater. Sci. Eng.: A 869 (2023) 144772, https://doi.org/10.1016/J.MSEA.2023.144772.

[64] T. Nakata, C. Xu, R. Ajima, K. Shimizu, S. Hanaki, T.T. Sasaki, L. Ma, K. Hono, S. Kamado, Strong and ductile age-hardening Mg-Al-Ca-Mn alloy that can be extruded as fast as aluminum alloys, Acta Mater. 130 (2017) 261–270, https://doi.org/10.1016/J.ACTAMAT.2017.03.046.

[65] J.J. Bhattacharyya, T.T. Sasaki, T. Nakata, K. Hono, S. Kamado, S.R. Agnew, Determining the strength of GP zones in Mg alloy AXM10304, both parallel and perpendicular to the zone, Acta Mater. 171 (2019) 231–239, https://doi.org/10.1016/J.ACTAMAT.2019.04.035.

[66] M. Bian, X. Huang, Y. Chino, Improving flame resistance and mechanical properties of magnesium–silver–calcium sheet alloys by optimization of calcium content, J. Alloy. Compd. 837 (2020) 155551, https://doi.org/10.1016/J.JALLCOM.2020.155551.

[67] T. Nakata, C. Xu, Y. Yoshida, K. Yoshida, S. Kamado, Improving room-temperature stretch formability of a high-alloyed Mg–Al–Ca–Mn alloy sheet by a high-temperature solution-treatment, Mater. Sci. Eng.: A 801 (2021) 140399, https://doi.org/10.1016/J.MSEA.2020.140399.

[68] Z.R. Zeng, Y.M. Zhu, S.W. Xu, M.Z. Bian, C.H.J. Davies, N. Birbilis, J.F. Nie, Texture evolution during static recrystallization of cold-rolled magnesium alloys, Acta Mater. 105 (2016) 479–494, https://doi.org/10.1016/J.ACTAMAT.2015.12.045.

[69] T.T.T. Trang, J.H. Zhang, J.H. Kim, A. Zargaran, J.H. Hwang, B.C. Suh, N.J. Kim, Designing a magnesium alloy with high strength and high formability, Nat. Commun. 9 (2018), https://doi.org/10.1038/s41467-018-04981-4.

[70] Y. Jin, C. Blawert, F. Feyerabend, J. Bohlen, M. Silva Campos, S. Gavras, B. Wiese, D. Mei, M. Deng, H. Yang, R. Willumeit-Römer, Time-sequential corrosion behaviour observation of micro-alloyed Mg-0.5Zn-0.2Ca alloy via a quasi-in situ approach, Corros. Sci. 158 (2019) 108096, https://doi.org/10.1016/J.CORSCI.2019.108096.

[71] X. Chen, F. Pan, J. Mao, J. Huang, Effect of impurity reduction on rollability of AZ31 magnesium alloy, J. Mater. Sci. 47 (2012) 514–520, https://doi.org/10.1007/s10853-011-5828-6.

[72] M.R. Barnett, Z. Keshavarz, A.G. Beer, D. Atwell, Influence of grain size on the compressive deformation of wrought Mg–3Al–1Zn, Acta Mater. 52 (2004) 5093–5103, https://doi.org/10.1016/J.ACTAMAT.2004.07.015.

[73] A. Jain, O. Duygulu, D.W. Brown, C.N. Tomé, S.R. Agnew, Grain size effects on the tensile properties and deformation mechanisms of a magnesium alloy, AZ31B, sheet, Mater. Sci. Eng.: A 486 (2008) 545–555, https://doi.org/10.1016/J.MSEA.2007.09.069.

[74] N. Stanford, M.R. Barnett, Effect of particles on the formation of deformation twins in a magnesium-based alloy, Mater. Sci. Eng.: A 516 (2009) 226–234, https://doi.org/10.1016/J.MSEA.2009.04.001.

[75] J. Jain, W.J. Poole, C.W. Sinclair, M.A. Gharghouri, Reducing the tension–compression yield asymmetry in a Mg–8Al–0.5Zn alloy via precipitation, Scr. Mater. 62 (2010) 301–304, https://doi.org/10.1016/J.SCRIPTAMAT.2009.11.024.

[76] N. Stanford, M.R. Barnett, Solute strengthening of prismatic slip, basal slip and $\{10\bar{1}2\}$ twinning in Mg and Mg–Zn binary alloys, Int J. Plast. 47 (2013) 165–181, https://doi.org/10.1016/J.IJPLAS.2013.01.012.

[77] S. Cai, T. Lei, N. Li, F. Feng, Effects of Zn on microstructure, mechanical properties and corrosion behavior of Mg–Zn alloys, Mater. Sci. Eng.: C. 32 (2012) 2570–2577, https://doi.org/10.1016/J.MSEC.2012.07.042.

[78] M.C. Merino, A. Pardo, R. Arrabal, S. Merino, P. Casajús, M. Mohedano, Influence of chloride ion concentration and temperature on the corrosion of Mg–Al alloys in salt fog, Corros. Sci. 52 (2010) 1696–1704, https://doi.org/10.1016/J.CORSCI.2010.01.020.

[79] E.V. Parfenov, O.B. Kulyasova, V.R. Mukaeva, B. Mingo, R.G. Farrakhov, Y. V. Cherneikina, A. Yerokhin, Y.F. Zheng, R.Z. Valiev, Influence of ultra-fine grain structure on corrosion behaviour of biodegradable Mg-1Ca alloy, Corros. Sci. 163 (2020) 108303, https://doi.org/10.1016/J.CORSCI.2019.108303.

[80] Y. Zhang, X. Feng, Q. Huang, Y. Li, X. Hao, C. Wang, Y. Yang, The corrosion characteristics and mechanism of directionally solidified Mg-3Zn-xCa alloys, J. Magnes. Alloy. 11 (2023) 3673–3687, https://doi.org/10.1016/J.JMA.2022.02.010.

[81] Y. Zhang, X. Feng, Q. Huang, Y. Li, Y. Yang, Effect of the microstructure parameters on the corrosion characteristics of Mg-Zn-Ca alloy with columnar structure, J. Magnes. Alloy. 11 (2023) 1709–1720, https://doi.org/10.1016/J.JMA.2021.12.017.

[82] G.L. Song, R. Mishra, Z. Xu, Crystallographic orientation and electrochemical activity of AZ31 Mg alloy, Electrochem Commun. 12 (2010) 1009–1012, https://doi.org/10.1016/J.ELECOM.2010.05.011.

[83] K. Hagihara, M. Okubo, M. Yamasaki, T. Nakano, Crystal-orientation-dependent corrosion behaviour of single crystals of a pure Mg and Mg-Al and Mg-Cu solid solutions, Corros. Sci. 109 (2016) 68–85, https://doi.org/10.1016/J.CORSCI.2016.03.019.

[84] B. Jiang, Q. Xiang, A. Atrens, J. Song, F. Pan, Influence of crystallographic texture and grain size on the corrosion behaviour of as-extruded Mg alloy AZ31 sheets, Corros. Sci. 126 (2017) 374–380, https://doi.org/10.1016/J.CORSCI.2017.08.004.

[85] S. Pawar, T.J.A. Slater, T.L. Burnett, X. Zhou, G.M. Scamans, Z. Fan, G. E. Thompson, P.J. Withers, Crystallographic effects on the corrosion of twin roll cast AZ31 Mg alloy sheet, Acta Mater. 133 (2017) 90–99, https://doi.org/10.1016/J.ACTAMAT.2017.05.027.

[86] N.N. Aung, W. Zhou, Effect of grain size and twins on corrosion behaviour of AZ31B magnesium alloy, Corros. Sci. 52 (2010) 589–594, https://doi.org/10.1016/J.CORSCI.2009.10.018.

[87] J. Liao, M. Hotta, N. Yamamoto, Corrosion behavior of fine-grained AZ31B magnesium alloy, Corros. Sci. 61 (2012) 208–214, https://doi.org/10.1016/J.CORSCI.2012.04.039.

[88] T. Zheng, Y. Hu, S. Yang, Effect of grain size on the electrochemical behavior of pure magnesium anode, J. Magnes. Alloy. 5 (2017) 404–411, https://doi.org/10.1016/J.JMA.2017.09.003.

[89] Y. Cheng, L. Zhao, Y. Xin, C. Yan, X.B. Chen, Q. Liu, P. Wu, Corrosion behavior of Mg-3Al-1Zn alloy with different grain refinement strategies, J. Mater. Sci. (2024), https://doi.org/10.1007/s10853-023-09315-4.

[90] Q. Xie, A. Ma, J. Jiang, H. Liu, Z. Cheng, Y. Gu, Tailoring the corrosion behavior and mechanism of AZ31 magnesium alloys by different Ca contents for marine

application, Corros. Sci. 192 (2021) 109842, https://doi.org/10.1016/J.CORSCI.2021.109842.